Japanese Journal of Applied Physics **53**, 05FB12 (2014) **REGULAR PAPER**
http://dx.doi.org/10.7567/JJAP.53.05FB12

Fabrication and crystal structure of [ABO_3/$REMO_3$] (A = Ca, La, B = Fe, Mn, RE = Bi, La, M = Fe, $Fe_{0.8}Mn_{0.2}$) superlattices grown by pulsed laser deposition method

Yuta Watabe[1], Nobuyuki Iwata[1], Takahiro Oikawa[1], Takuya Hashimoto[2], Mark Huijben[3], Guus Rijnders[3], and Hiroshi Yamamoto[1]

[1]*College of Science and Technology, Nihon University, Funabashi, Chiba 274-8501, Japan*
[2]*College of Humanities and Sciences, Nihon University, Setagaya, Tokyo 156-8550, Japan*
[3]*Faculty of Science and Technology and MESA+ Institute for Nanotechnology, University of Twente, 7500 AE Enschede, The Netherlands*

Received November 4, 2013; revised January 30, 2014; accepted February 5, 2014; published online April 16, 2014

In this study, we aim to synthesize novel materials that show ferromagnetic and ferroelectric properties with the magnetoelectric effect at room temperature. Nine types of superlattice were fabricated by stacking [7 units — ABO_3/7 units — $REMO_3$] for 14 times by pulsed laser deposition. From all reciprocal space mappings (RSMs) of the $CaMnO_3$ (CMO) superlattices, the satellite peaks were clearly observed. The calculated in-plain lattice parameter was 0.382 nm longer than 0.3732 nm, which is the bulk CMO and in-plain lattice parameter of the CMO thin film grown on $SrTiO_3$ (001) substrate. All the $CaFeO_3$ (CFO) series superlattices showed that the satellite peaks and Laue oscillations were clearly observed from the XRD 2θ–θ spectra. In the case of [CFO/$BiFeO_3$ (BFO)] superlattices, the number of deposited units of CFO in [CFO/BFO] one cycle was 6.94, which was quite close to the seven units that we aimed. The in-plain lattice constant of all the CFO series superlattices was fitted to that of the substrate. From RSMs of the [$LaMnO_3$ (LMO)/BFO] superlattice, the lattice parameter of the superlattice was fitted to that of the substrate in-plain. The cube-on-cube growth was confirmed in these LMO series superlattices. © 2014 The Japan Society of Applied Physics

1. Introduction

In the $SrTiO_3$ (STO)/$LaAlO_3$ (LAO) multilayer when LAO is deposited on a TiO_2-terminated STO substrate, n-type conduction at the interface is induced. At a low temperature, superconductivity[1–3] appeared and ferromagnetic[4–8] ordering is indicated as well. In the STO perovskite structure, SrO and TiO_2 charge neutral layers are stacking sequentially, while in the LAO pseudo perovskite structure, positive charge state of LaO and negative charge state of AlO_2 layers are stacked.[9–18] One of the reasons why the n-type conduction appears is the net transfer of electrons through the interface to reduce the electric potential caused by the polar/nonpolar interface, polar discontinuity.

In this study, we aim to synthesize the novel materials that show ferromagnetic (FM) and ferroelectric (FE) properties with the magnetoelectric (ME) effect at room temperature.[11–15] We expect an induced ferromagnetic ordering near the interface in the [ABO_3/$REMO_3$] (A = Ca, La, B = Fe, Mn, RE = Bi, La, M = Fe, $Fe_{0.8}Mn_{0.2}$) superlattices. Since the magnetic ordering of $BiFeO_3$ (BFO) is antiferromagnetic, the induced ferromagnetic ordering is expected owing to the electron transfer. When the electron transfers, we expect that the superexchange interaction between iron ions in BFO changes from antiferromagnetic to ferromagnetic following the construction of the $3d^5$ (Fe^{3+})–O–$3d^4$ (Fe^{4+}) straight bond according to the Kanomori–Goodenough rule.[19–23] In this research, we focus on the fabrication and structure analysis of the [ABO_3/$REMO_3$] superlattices.

2. Experimental methods

Nine types of superlattice were grown by the alternate stacking of the materials *A* and the materials *B* using pulsed laser deposition (PLD) with an excimer laser of KrF 248 nm on STO(001) substrates, where the materials *A* are BFO, $BiFe_{0.8}Mn_{0.2}O_3$ (BFMO), and $LaFeO_3$ (LFO), and the materials *B* are $CaMnO_3$ (CMO), $CaFeO_3$ (CFO) and $LaMnO_3$ (LMO). The superlattices were fabricated by stacking [7 units — ABO_3/7 units — $REMO_3$] for 14 times. High-density LFO (95.48%) and CFO (96.38%) targets were particularly prepared by the Pechini method.[24–26] The other targets of CMO, LMO, BFO, and BFMO were calcined by the traditional solid-state reaction method. The STO(001) substrate was ultrasonically cleaned in acetone and ethanol. The cleaned substrate was soaked in pure water for 30 min in an ultrasonic bath. The substrate surface was etched using a commercial buffered hydrogen fluoride (BHF) (Daikin Industries, pH = 5.0) for 30 s, and immediately rinsed using pure water. The etched substrate was annealed at 920 °C for 6 h in air. The deposited condition was as follows: 670 °C heater temperature, 2.5–2.8 J/cm^2 energy density at the target surface, 4 Hz repetition rate, and 20 Pa oxygen atmosphere during growth.

Since we demonstrated the layer-by-layer growth of LFO with a step-terrace surface structure and a stable growth rate using a high-density target prepared by the Pechini method up to 135 units, end of the growth,[27] the growth rate ratios of LFO to other films were investigated in advance by depositing all the materials *A* and *B* on seven units of the LFO calibration layer for the accurate control of each deposition thickness in superlattice growth. When the superlattices were prepared, seven units of LFO film were deposited first, and the required pulses for other materials to grow seven units were calculated using the growth rate ratio and the growth rate of the last three units of LFO.

All the films were evaluated by reflection high energy electron diffraction (RHEED), X-ray diffraction (XRD), X-ray reflection (XRR), and reciprocal space mapping (RSM) using a one-dimensional detector (VÅNTEC-1) in Bruker D8 Discover. The surface morphology was investigated by scanning probe microscopy (SPM).

3. Results

3.1 Calibration of superlattices growth

Figure 1 shows the RHEED oscillation and growth time for one unit of the initial seven units of LFO. The growth rate was quite stable during growth. The ratios of required pulses for other films were calculated from the last three stable oscillations, as indicated by closed circles. Table I shows the results of the ratios of required pulses of LFO to other films.

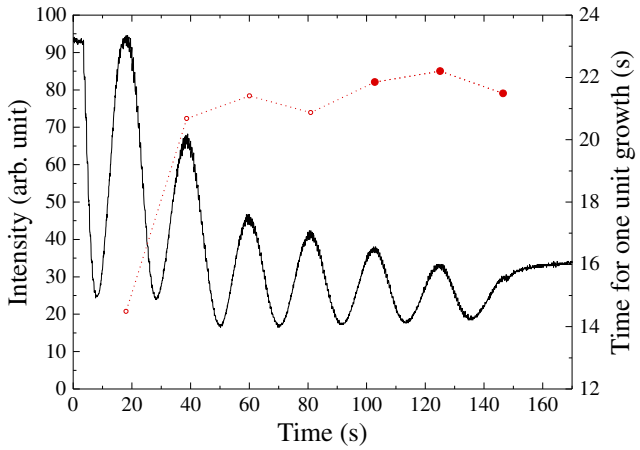

Fig. 1. (Color online) RHEED oscillation (solid line in the left vertical) and time for one unit growth of LFO seven units (red dotted line in the right vertical) using targets prepared by the Pechini method. The time was calculated from the period between oscillation peaks. The ratios of required pulses for other films were calculated from the last three stable oscillations (closed circles).

Table I. Required pulse ratios to grow seven units compared with that of LFO.

CMO	CFO	LMO	BFO	BFMO
0.532	0.699	0.563	1.01	0.720

From the ratios, we determined the number of pulses to deposit seven units for each material in superlattices.

3.2 $CMO/REMO_3$ series superlattices

Figure 2 shows the RHEED patterns and surface morphologies of the (a) [CMO/BFO], (b) [CMO/BFMO], and (c) [CMO/LFO] superlattices. All the CMO superlattice surfaces showed basically a step-terrace structure, although some grains outgrew on the surface with the height of 10–15 nm. The RHEED pattern was streaky in [CMO/LFO], but streak + spots were observed in the [CMO/BFO] and [CMO/BFMO] superlattices. The streak and spots were caused by the smooth surface and the outgrowth on the surface.

The XRD 2θ–θ spectra of the CMO series superlattices around STO(001) or STO(002) substrate peaks are shown in Fig. 3. The satellite peaks (SLs) and Laue oscillations were clearly observed. The SLs were numbered in the figure. The thickness of one cycle [7 units — CMO/7 units — $REMO_3$] (T_{CYCLE}) of the superlattices, average lattice constant (L_{AVE}), and total film thickness (L_{TOTAL}) were calculated from the SLs period, from the 2θ position of the peaks noted by "0" by fitting using the Nelson-Riley function, and from 14 times of the T_{CYCLE}, respectively. The full width at half maximum (FWHM) was of the rocking curve. Those values are summarized in Table II. Figure 4 shows the XRR spectra of the (a) [CMO/BFO], (b) [CMO/BFMO], and (c) [CMO/LFO] superlattices with the fitting results denoted by the dotted lines. The short-period and long-period oscillations are derived from the film thickness and superstructure, respectively. From the fitting result, each film thickness of the [7 units — CMO/7 units — $REMO_3$] and the T_{CYCLE} were estimated. The number of deposited units for one cycle was calculated using the lattice constant of the single layer. L_{AVE} was calculated by the T_{CYCLE} divided using total deposited number of units of CMO and $REMO_3$. Those values are summarized in Table II as well.

Although the required pulses to deposit seven units for superlattice growth were accurately estimated, the number of deposited units was definitely less than seven, roughly from 5.2 to 6.3 units. It is unclear why the growth method for superlattices did not work at this moment. However, the estimated values from the results of XRD and XRR were consistent quite accurately. It is expected that the cation intermixing around the interface involves one or two units.

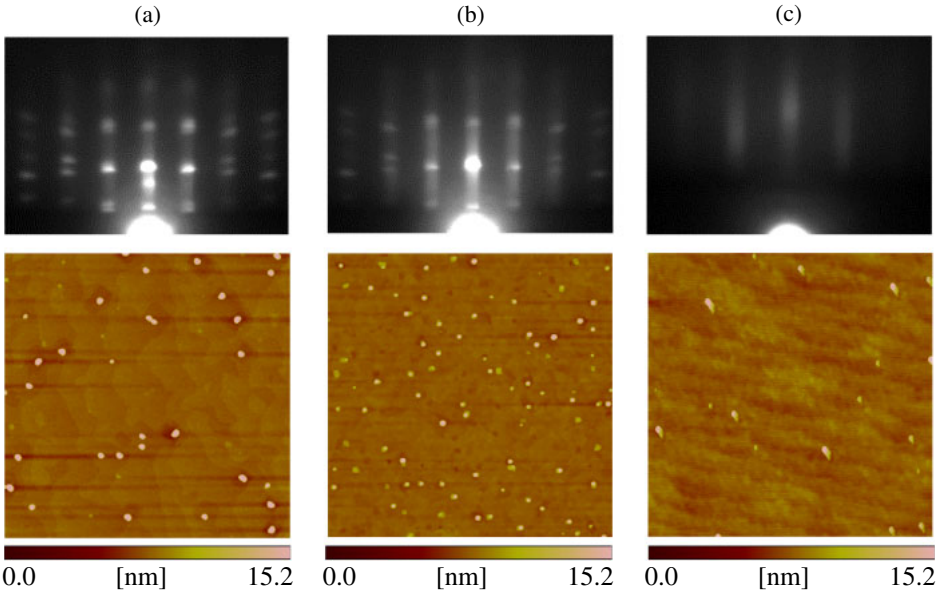

Fig. 2. (Color online) RHEED patterns along STO[100] direction after deposition (top figures) and surface morphologies with size of $2 \times 2\,\mu m^2$ (bottom figures) of (a) [CMO/BFO], (b) [CMO/BFMO], and (c) [CMO/LFO] superlattices.

Table II. Summary table from results of XRD and XRR.

		[CMO/BFO]	[CMO/BFMO]	[CMO/LFO]
XRD	Thickness of each cycle, T_{CYCLE} (nm)	4.78	4.12	4.76
	Average lattice constant, L_{AVE} (nm)	0.3847	0.3896	0.3821
	Total film thickness, T_{TOTAL} (nm)	66.9	57.7	66.4
	FWHM (deg)	0.0736	0.0749	0.0974
XRR	Number of deposited units for one cycle			
	A, LFO, BFO, BFMO	5.93	5.27	6.14
	B, CMO	6.33	5.48	5.37
	Thickness of each cycle, T_{CYCLE} (nm)	4.77	4.18	4.44
	Average lattice constant, L_{AVE} (nm)	0.3892	0.3890	0.3854
	Total film thickness, T_{TOTAL} (nm)	66.8	58.5	66.1

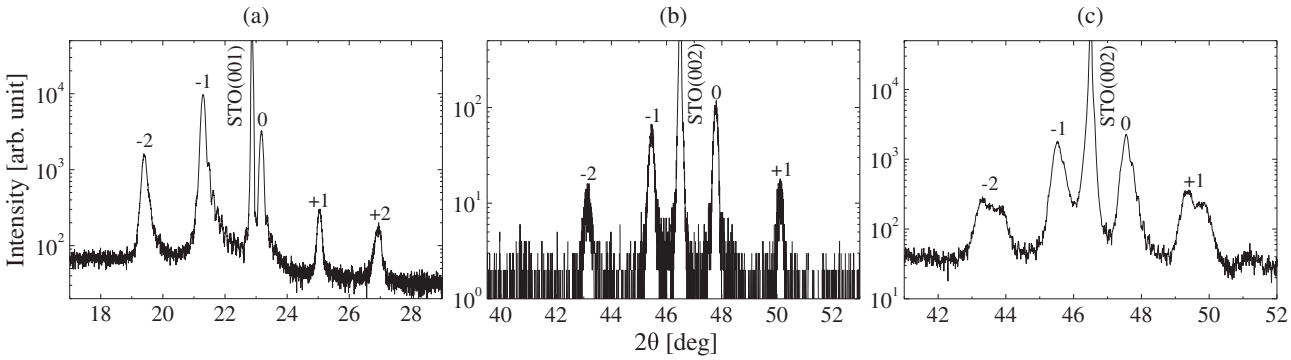

Fig. 3. XRD patterns of (a) [CMO/BFO], (b) [CMO/BFMO], and (c) [CMO/LFO] superlattices around the STO(001) or STO(002) substrate peak. The satellite peaks and Laue oscillations were observed. The SLs were numbered in the figure.

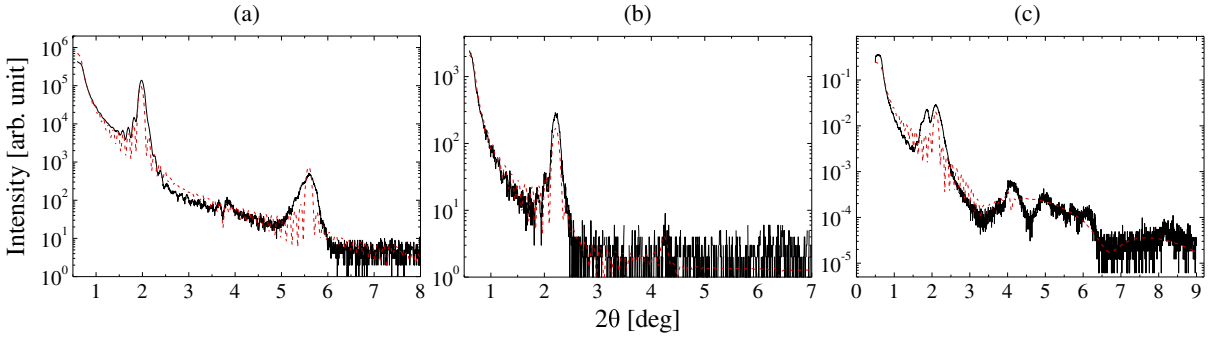

Fig. 4. (Color online) XRR spectra with fitting results denoted by the dotted lines. The short-period and long-period oscillations are derived from the film thickness and superstructure.

The RSMs of [CMO/BFMO] superlattice around (a) STO(003), (b) STO(103), and (c) STO(113) peaks are shown in Fig. 5. Similar RSM results were obtained in the [CMO/BFO] and [CMO/LFO] superlattices. The SLs were clearly observed in all RSMs. The calculated in-plain lattice parameter was 0.382 nm, longer than 0.3732 nm, which is the bulk CMO[28] and in-plain lattice parameter of the CMO thin film grown on STO(001) substrate. While the lattice parameter was 2.3% longer than that of the substrate, the RSM results revealed a cube-on-cube crystal growth.

3.3 CFO/REMO$_3$ series superlattices

Figure 6 shows the RHEED patterns and surface morphologies of the (a) [CFO/BFO], (b) [CFO/BFMO], and (c) [CFO/LFO] superlattices. All the CFO series superlattices a showed smooth surface with a step-terrace structure. The RHEED pattern was streaky, indicating the smooth surface.

The XRD 2θ–θ spectra of the (a) [CFO/BFO], (b) [CFO/BFMO], and (c) [CFO/LFO] superlattices around the STO(001) or STO(002) substrate peak are shown in Fig. 7. The SLs and Laue oscillations were clearly observed. In the case of [CFO/BFO] superlattices, the SLs from -4 to $+4$ were observed. The values of T_{CYCLE}, L_{AVE}, and L_{TOTAL}, were calculated at 4.75, 0.3848, and 66.5 nm, respectively. From the fitting result to the XRR spectrum, the values of T_{CYCLE}, L_{AVE}, and L_{TOTAL} were calculated at 4.73, 0.3856, and 66.2 nm, respectively. Those calculated values corresponded

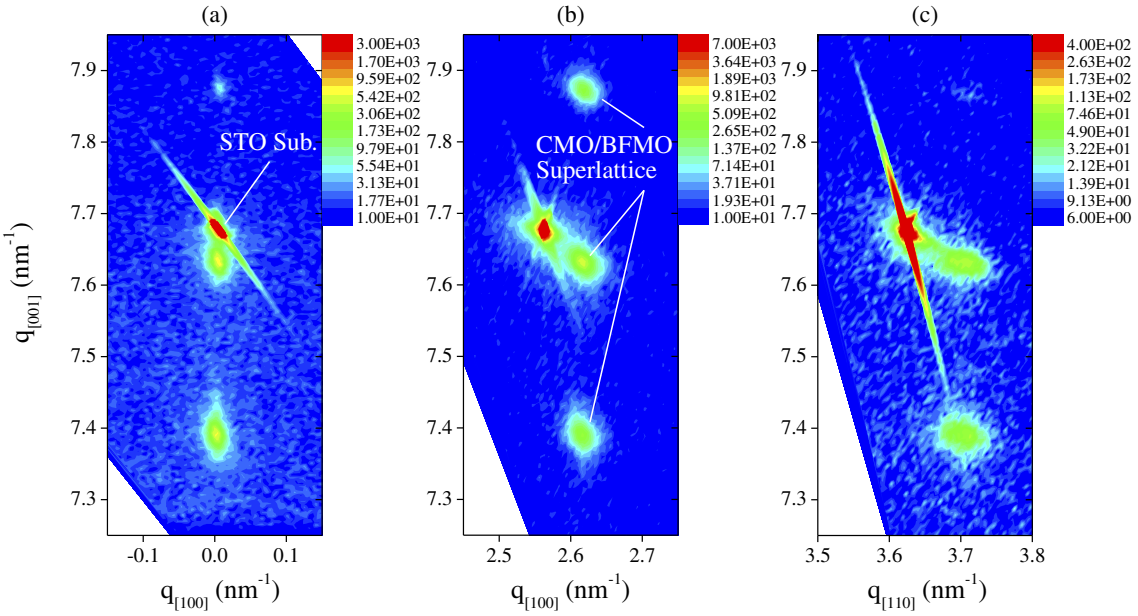

Fig. 5. (Color online) RSMs of [CMO/BFMO] superlattice around (a) STO(103) and (b) STO(113). The in-plain lattice parameter of the superlattice was not fitted to the STO substrate. The calculated in-plain lattice parameter was 2.3% longer than that of the substrate.

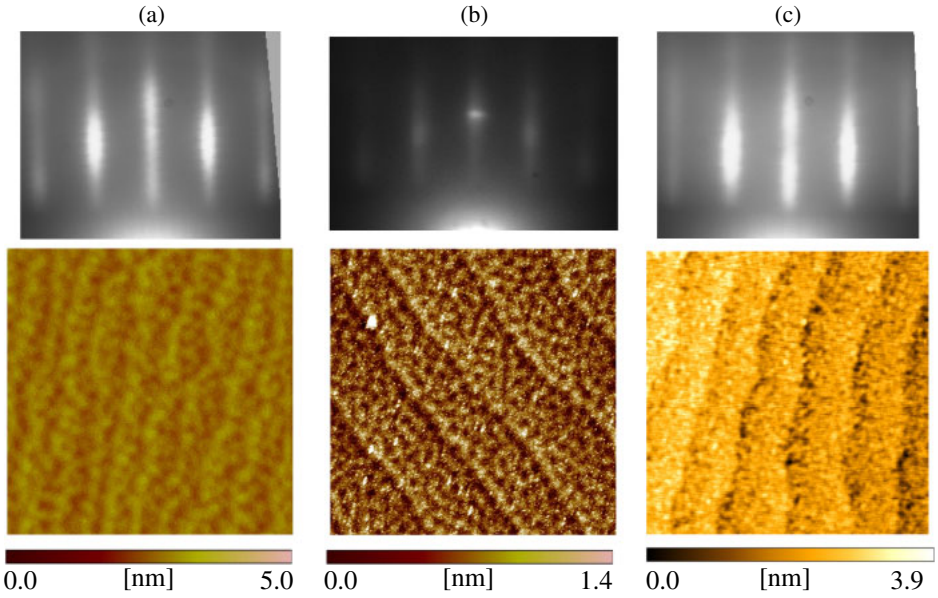

Fig. 6. (Color online) RHEED patterns along STO[100] direction after deposition (top figures) and surface morphologies with the size of 5 × 5 μm^2 (bottom figures) of (a) [CFO/BFO], (b) [CFO/BFMO], and (c) [CFO/LFO] superlattices.

to each other within 1%. In particular, the number of deposited units of CFO in [CFO/BFO] one cycle was 6.94, which was quite close to the seven units that we aimed. The XRR spectra of [CFO/BFMO] and [CFO/LFO] were not suitable to fit successfully because of the gold passivation layer on top of the superlattices.

Figure 8 shows the RSMs of the [CFO/BFMO] superlattice around the (a) STO(003), (b) STO(103), and (c) STO(113). The SLs as well as Laue oscillations were clearly observed. The in-plain lattice constants of all the CFO series superlattices were fitted to that of the substrate. Since the crystal structure of the single layer of BFO and BFMO on STO(001) is monoclinic and tilted orthorhombic or rhombohedral, the strong compressive stress was forced in BFO and BFMO layers in the superlattice.[29] The cube-on-cube growth of superlattices was realized, and the very good superstructure and crystallinity of [CFO/BFO] were demonstrated by the SLs from −4 to +4 and Laue oscillation.

3.4 LMO/REMO$_3$ series superlattices

Figure 9 shows the RHEED patterns and surface morphologies of the (a) [LMO/BFO], (b) [LMO/BFMO], and (c) [LMO/LFO] superlattices. All the LMO series superlattices surfaces showed a step-terrace structure. The streaky RHEED pattern somewhat indicated a smooth surface. However, many facets were observed in the (a) [LMO/BFO] and (b)

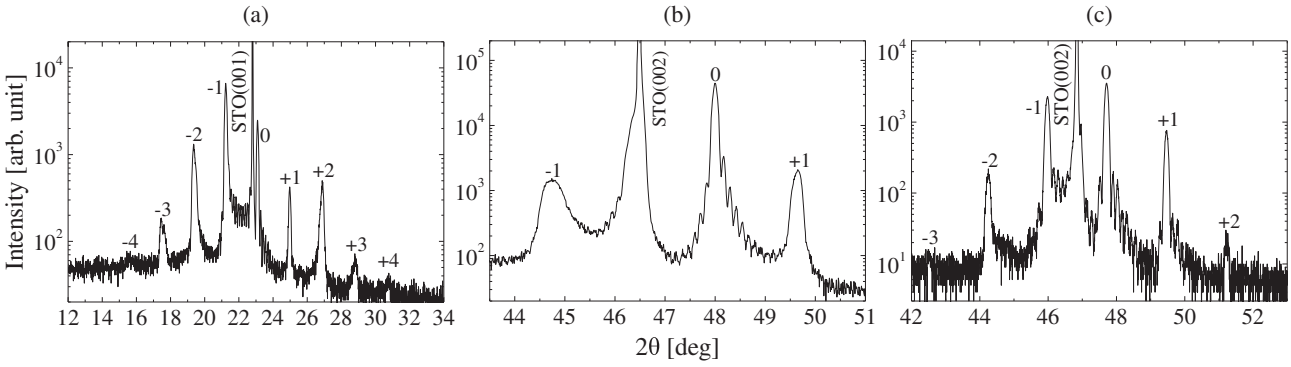

Fig. 7. XRD pattern of (a) [CFO/BFO], (b) [CFO/BFMO], and (c) [CFO/LFO] superlattices around STO(001) or STO(002) substrate peak. The SLs and Laue oscillations were clearly observed.

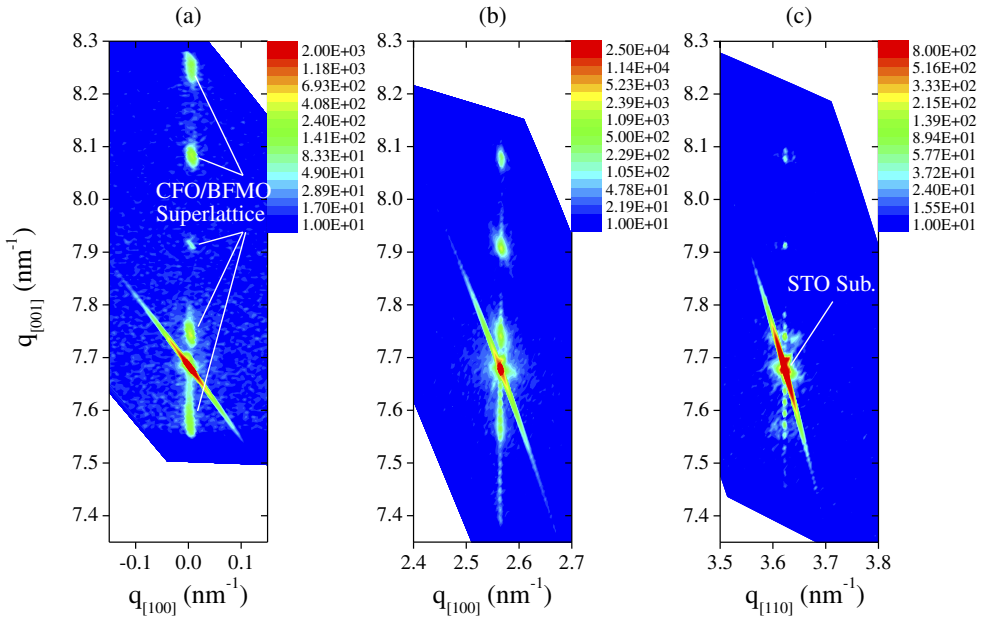

Fig. 8. (Color online) RSMs of [CFO/BFMO] superlattice around (a) STO(003), (b) STO(103), and (c) STO(113). The in-plain lattice parameter of the superlattice was fitted to the STO substrate.

[LMO/BFMO] superlattices. In addition, two extra streaks were faintly observed between (00) and (10) or $(\bar{1}0)$ in the (b) [LMO/BFMO] superlattice, probably due to the anisotropic grains on the surface. An intermediate streak can also be seen in the (c) [LMO/LFO] superlattices, indicating the reconstruction at the surface with a doubled period.

The XRD 2θ–θ spectra of the (a) [LMO/BFO], (b) [LMO/BFMO], and (c) [LMO/LFO] superlattices around the STO(002) or STO(004) substrate peak are shown in Fig. 10. In Table III, the L_{AVE} and FWHM are summarized. Except for (c), the crystalline structure was not good. In the case of (c) [LMO/LFO] superlattices, the Laue oscillation and SLs from -1 to $+1$ were observed. The values of T_{CYCLE} and L_{TOTAL} were calculated at 4.97 and 69.5 nm, respectively.

Figure 11 shows the RSMs of the [LMO/BFO] superlattice around the (a) STO(003), (b) STO(103), and (c) STO(113). The SLs were detected. The lattice parameter of the superlattice was fitted to that of the substrate in-plain. The cube-on-cube growth was confirmed in these LMO series superlattices as well.

4. Discussion

Almost all the synthesized superlattices exhibited a step-terrace structure at the surface and the SLs and Laue oscillation in the XRD measurements. Those results indicate that the superstructure with a smooth interface is synthesized. However, each superlattice showed different structural properties. The major reasons are expected to be differences in (i) lattice mismatch and (ii) degree of crystal symmetry. There are two types of lattice mismatch summarized in Table IV. One is lattice mismatch between ABO_3 and $REMO_3$, described at the upper row in the crossed cells. The other one is the lattice mismatch between the average lattice constants of ABO_3 and $REMO_3$ and that of the substrate, described at the lower row in the crossed cells.

In the case of [CMO/BFO] and [CMO/BFMO] superlattices, the appearance of the outgrowth is expected to be due to the large difference in the lattice constant between CMO and $REMO_3$ and the low crystal symmetries of the rhombohedral BFO and BFMO, as shown in Figs. 2(a) and

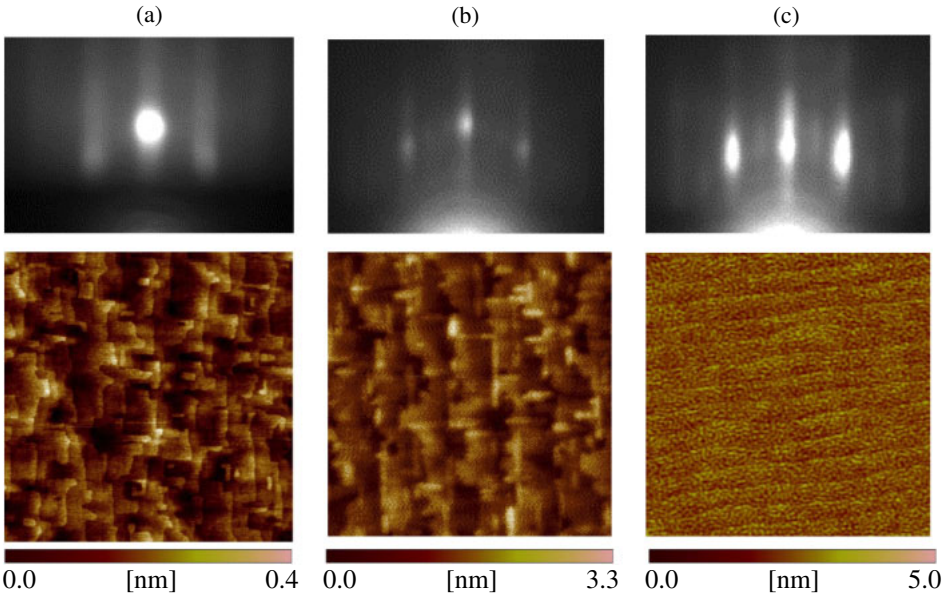

Fig. 9. (Color online) RHEED pattern along STO[100] direction after deposition (top figures) and surface morphologies with the size of $2 \times 2\,\mu m^2$ (bottom figures) of (a) [LMO/BFO], (b) [LMO/BFMO], and (c) [LMO/LFO] superlattices. All LMO series superlattice surfaces showed a step-terrace structure. The streaky RHEED pattern somewhat indicated a smooth surface.

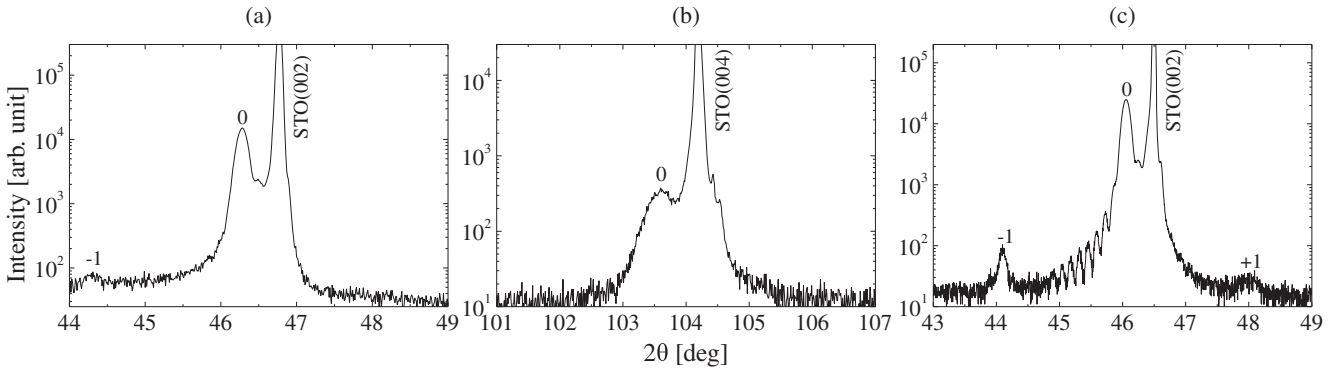

Fig. 10. The XRD patterns of (a) [LMO/BFO], (b) [LMO/BFMO], and (c) [LMO/LFO] superlattices around the STO(002) or STO(004) substrate peak.

Table III. Summary table from XRD results of $LMO/REMO_3$ series superlattices.

	[LMO/BFO]	[LMO/BFMO]	[LMO/LFO]
Average lattice constant, L_{AVE} (nm)	0.3944	0.3922	0.3941
FWHM (deg)	0.110	0.197	0.0753

Table IV. Lattice mismatches using lattice constant of pseudocubic structure calculated from the values reported in Refs. 7, 28, 31–33. The values in parentheses are the mismatch of each single crystal compared with that of the substrate. At the crossed cell, the mismatch value between ABO_3 and $REMO_3$ is described in the upper row. The mismatch of the average lattice constant of ABO_3 and $REMO_3$ compared with that of the substrate is also described in the lower row.

	Lattice mismatch	BFO (+2.52%)	BFMO (+1.11%)	LFO (+0.655%)
CMO	(−4.45%)	6.98% −0.965%	5.57% −1.67%	5.11% −1.90%
CFO	(−3.36%)	5.89% −0.419%	4.47% −1.13%	4.02% −1.35%
LMO	(+1.01%)	1.51% 1.77%	0.0989% 1.06%	0.357% 0.833%

2(b). The rhombohedral BFO and BFMO tend to tilt to be monoclinic as the films are grown on the STO substrate. On such BFO and/or BFMO film, orthorhombic CMO might grow with space for outgrowth. The grains of the outgrowth attract surplus atoms for the superlattice growth, resulting in the appearance of the step-terrace structures. The surface of the [CMO/LFO] superlattice showed a step-terrace structure with reduced number of outgrowth, which is due to the crystal symmetry of orthorhombic LFO, as shown in Fig. 2(c).

The lattice mismatch between CFO and BFO is large, but the average lattice constants of CFO and BFO are almost the same as that of the substrate to order the lattice in-plain in the case of the [CFO/BFO] superlattice. Those circumstances demonstrated the step-terrace structure without outgrowth and the clear SLs and Laue oscillation as shown

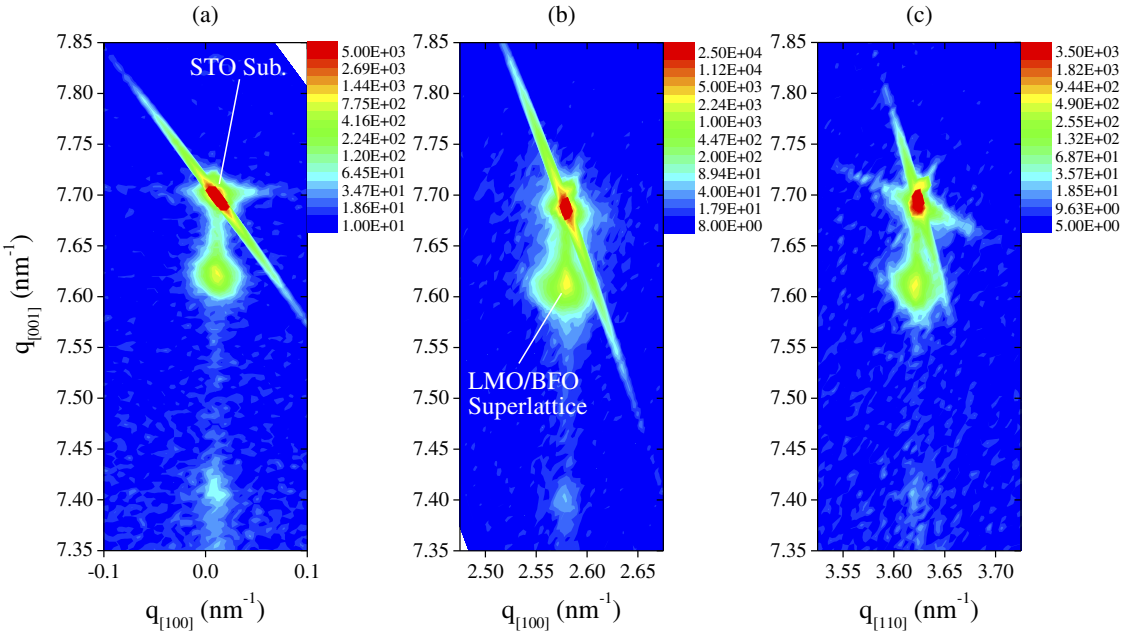

Fig. 11. (Color online) RSMs of [LMO/BFO] superlattice around (a) STO(003), (b) STO(103), and (c) STO(113). The in-plain lattice parameter of the superlattice was fitted to the STO substrate.

in Figs. 6(a) and 7(b). The other CFO series superlattices have a similar circumstance, resulting in the excellent superstructure with a smooth surface as shown in Figs. 6(b), 6(c), 7(b), and 7(c).

In the meantime, the lattice constants of both LMO and $REMO_3$ are larger than those of the substrate in the LMO series superlattices. As shown in Table IV, the lattice mismatch between LMO and $REMO_3$ is smaller than those of other superlattices, but the average lattice constant is always larger than that of the substrate. Considering that the film surface of single BFO and BFMO layers on STO substrate is formed by rectangular grains, it is reasonable to show a lot of facets with a step-terrace structure for the [LMO/BFO] and [LMO/BFMO] superlattices, as shown in Figs. 9(a) and 9(b), respectivery. However, in the case of the [LMO/LFO] superlattice, both single layers of LMO and LFO show RHEED oscillation and the step-terrace surface, indicating that the superlattice could have fine structure. Since the densities of the LMO and LFO are similar, the SL appearance must be poor. In addition, the observation of Laue oscillation and sharp FWHM reveal the good quality of the superlattice.

5. Conclusion

In this study, we aim to synthesize novel materials that shows FM and FE properties with the ME effect at room temperature. Nine types of superlattice were grown by the alternate stacking of materials *A* of LFO, BFO, and BFMO, and materials *B* of CMO, CFO, and LMO by PLD. When the superlattices were prepared, an LFO film of seven units was seven units of LFO film were deposited first, and the required pulses for other materials to grow seven units were calculated.

All the CMO superlattice surfaces showed basically a step-terrace structure, a though some grains outgrew on the surface with the height of 10–15 nm. The RHEED pattern was streaky in [CMO/LFO], but streak + spots were observed in the [CMO/BFO] and [CMO/BFMO] superlattices. From all RSMs of the CMO superlattices, the SLs were clearly observed. The calculated in-plain lattice parameter was 0.382 nm, longer than 0.3732 nm, which is the bulk CMO and in-plain lattice parameter of CMO thin film grown on STO(001) substrate. While the lattice parameter was 2.3% longer than that of the substrate, the RSM results revealed a cube-on-cube crystal growth.

All CFO series superlattices showed a smooth surface with a step-terrace structure. The RHEED pattern was streaky, indicating the smooth surface. From the XRD 2θ–θ spectra, the SLs and Laue oscillations were clearly observed. In the case of [CFO/BFO] superlattices, the SLs from -4 to $+4$ were observed. In particular, the number of deposited units of CFO in [CFO/BFO] one cycle was 6.94, which was quite close to the seven units that we aimed. The in-plain lattice constant of all the CFO series superlattices was fitted to that of the substrate. Since the crystal structure of the single layers of BFO and BFMO on STO(001) is monoclinic and tilted orthorhombic or rhombohedral, the strong compressed stress was forced in the BFO and BFMO layer in the superlattice.

All the LMO series superlattice surfaces showed a step-terrace structure. The streaky RHEED pattern somewhat indicated a smooth surface. In the XRD 2θ–θ spectra of the [LMO/LFO] superlattices, the Laue oscillation and SLs from -1 to $+1$ were observed. The value of T_{CYCLE} and L_{TOTAL} were calculated at 4.97 and 69.5 nm, respectively. In the case of the [LMO/BFO] superlattice, the lattice parameter of the superlattice was fitted to that of the substrate in-plain. The cube-on-cube growth was confirmed in these LMO series superlattices as well.

The structural differences are expected to be attributed from the differences in (i) lattice mismatch and (ii) degree of crystal symmetry. The superlattice including low crystal symmetry of BFO and/or BFMO showed rather rough

surfaces: outgrowth in [CMO/BFO, BFMO] superlattices and a lot of facets in [LMO/BFO, BFMO] superlattices. However, the CFO series and [LMO/LFO] superlattices showed a clear step-terrace surface; the SLs and Laue oscillation are probably due to the small lattice mismatch between the average lattice constant and that of the substrate.

Acknowledgments

This study was supported by a Grant-in-Aid for Scientific Research (C), JSPS KAKENHI 25420295, Nihon University Multidisciplinary Research Grant for 2013, and CASIO Science promotion foundation.

1) N. Reyren, S. Thiel, A. D. Caviglia, L. F. Kourkoutis, G. Hammerl, C. Richter, C. W. Schneider, T. Kopp, A.-S. Rüetschi, D. Jaccard, M. Gabay, D. A. Muller, J.-M. Triscone, and J. Mannhart, Science **317**, 1196 (2007).
2) A. Ohtomo, D. A. Muller, J. L. Grazul, and H. Y. Hwang, Nature **419**, 378 (2002).
3) S. A. Pauli and P. R. Willmott, J. Phys.: Condens. Matter **20**, 264012 (2008).
4) M. Fiebig, J. Phys. D **38**, R123 (2005).
5) N. A. Hill, J. Phys. Chem. B **104**, 6694 (2000).
6) N. A. Hill and A. Filippetti, J. Magn. Magn. Mater. **242–245**, 976 (2002).
7) J. Wang, J. B. Neaton, H. Zheng, V. Nagarajan, S. B. Ogale, B. Liu, D. Viehland, V. Vaithyanathan, D. G. Schlom, U. V. Waghmare, N. A. Spaldin, K. M. Rabe, M. Wuttig, and R. Ramesh, Science **299**, 1719 (2003).
8) D. A. Dikin, M. Mehta, C. W. Bark, C. M. Folkman, C. B. Eom, and V. Chandrasekhar, Phys. Rev. Lett. **107**, 056802 (2011).
9) A. Ohtomo and H. Y. Hwang, Nature **427**, 423 (2004).
10) N. Nakagawa, H. Y. Hwang, and D. A. Muller, Nat. Mater. **5**, 204 (2006).
11) M. Huijben, G. Rijnders, D. H. A. Blank, S. Bals, S. V. Aert, J. Verbeeck, G. V. Tendeloo, A. Brinkman, and H. Hilgenkamp, Nat. Mater. **5**, 556 (2006).
12) M. Huijben, A. Brinkman, G. Koster, G. Rijnders, H. Hilgenkamp, and D. H. A. Blank, Adv. Mater. **21**, 1665 (2009).
13) M. R. Fitzsimmons, N. W. Hengartner, S. Singh, M. Zhernenkov, F. Y. Bruno, J. Santamaria, A. Brinkman, M. Huijben, H. J. A. Molegraaf, J. de la Venta, and I. K. Schuller, Phys. Rev. Lett. **107**, 217201 (2011).
14) F. Gunkel, P. Brinks, S. Hoffmann-Eifert, R. Dittmann, M. Huijben, J. E. Kleibeuker, G. Koster, G. Rijnders, and R. Waser, Appl. Phys. Lett. **100**, 052103 (2012).
15) R. Pentcheva, M. Huijben, K. Otte, W. E. Pickett, J. E. Kleibeuker, J. Huijben, H. Boschker, D. Kockmann, W. Siemons, G. Koster, H. J. W. Zandvliet, G. Rijnders, D. H. A. Blank, H. Hilgenkamp, and A. Brinkman, Phys. Rev. Lett. **104**, 166804 (2010).
16) W. Siemons, M. Huijben, G. Rijnders, D. H. A. Blank, T. H. Geballe, M. R. Beasley, and G. Koster, Phys. Rev. B **81**, 241308(R) (2010).
17) S. Thiel, G. Hammert, A. Schmehl, C. W. Schneider, and J. Mannhart, Science **313**, 1942 (2006).
18) Y. Segal, J. H. Ngai, J. W. Reiner, F. J. Walker, and C. H. Ahn, Phys. Rev. B **80**, 241107 (2009).
19) E.-M. Choi, S. Patnaik, E. Weal, S.-L. Sahonta, H. Wang, Z. Bi, J. Xiong, M. G. Blamire, Q. X. Jia, and J. L. Macmanus-Driscoll, Appl. Phys. Lett. **98**, 012509 (2011).
20) A. A. Belik, A. M. Abakumov, A. A. Tsirlin, J. Hadermann, J. Kim, G. Van Tendeloo, and E. Takayama-Muromachi, Chem. Mater. **23**, 4505 (2011).
21) J. Kanamori, J. Phys. Chem. Solids **10**, 87 (1959).
22) J. B. Goodenough, Phys. Rev. **100**, 564 (1955).
23) J. B. Goodenough, J. Phys. Chem. Solids **6**, 287 (1958).
24) M. P. Pechini, U.S. Patent 3330697 (1963).
25) E. Niwa, C. Uematsu, E. Miyashita, T. Ohzeki, and T. Hashimoto, Solid State Ionics **201**, 87 (2011).
26) Y. Tsuchiya, K. Norota, Y. Watabe, T. Kuroda, N. Iwata, T. Hashimoto, and H. Yamamoto, Trans. Mater. Res. Soc. Jpn. **37**, 369 (2012).
27) N. Iwata, Y. Watabe, Y. Tsuchiya, K. Norota, M. Huijben, G. Rijnders, D. H. A. Blank, and H. Yamamoto, Trans. Mater. Res. Soc. Jpn. **37**, 381 (2012).
28) I. G. de Muro, M. Insausti, L. Lezama, and T. Rojo, J. Solid State Chem. **178**, 928 (2005).
29) N. Iwata, T. Oikawa, Y. Watabe, and H. Yamamoto, in preparation for publication.
30) M. Azuma, H. Kanda, A. A. Belik, Y. Shimakawa, and M. Takano, J. Magn. Magn. Mater. **310**, 1177 (2007).
31) P. M. Woodward, D. E. Cox, E. Moshopoulou, A. W. Sleight, and S. Morimoto, Phys. Rev. B **62**, 844 (2000).
32) S. E. Dann, D. B. Currie, M. T. Weller, M. F. Thomas, and A. D. Al-Rawwas, J. Solid State Chem. **109**, 134 (1994).
33) B. Dabrowski, S. Kolesnik, A. Baszczuk, O. Chmaissem, T. Maxwell, and J. Mais, J. Solid State Chem. **178**, 629 (2005).